

The WISSH quasars project

VIII. Outflows and metals in the circum-galactic medium around the hyper-luminous $z \sim 3.6$ quasar J1538+08^{★,★★}

A. Travascio^{1,2,3}, L. Zappacosta¹, S. Cantalupo⁴, E. Piconcelli¹, F. Arrigoni Battaia^{5,6}, M. Ginolfi⁷, M. Bischetti¹, G. Vietri⁸, A. Bongiorno¹, V. D’Odorico^{9,10}, F. Duras¹¹, C. Feruglio⁹, C. Vignali^{12,13}, and F. Fiore⁹

¹ INAF-Osservatorio Astronomico di Roma, Via Frascati 33, 00078 Monteporzio Catone, Italy
e-mail: andrea.travascio@inaf.it

² Department of Physics, University of Rome “Tor Vergata”, Via della Ricerca Scientifica 1, 00133 Rome, Italy

³ Università degli Studi di Roma “Sapienza”, Piazzale Aldo Moro 5, 00185 Roma, Italy

⁴ Department of Physics, ETH Zurich, Wolfgang-Pauli-Strasse 27, 8093 Zurich, Switzerland

⁵ European Southern Observatory, Karl-Schwarzschild-Str. 2, 85748 Garching bei Munchen, Germany

⁶ Max-Planck-Institut für Astrophysik, Karl-Schwarzschild-Str 1, 85748 Garching, Germany

⁷ Observatoire de Genève, Université de Genève, 51 Ch. des Maillettes, 1290 Versoix, Switzerland

⁸ INAF, Istituto di Astrofisica Spaziale e Fisica Cosmica – Milano, Via A. Corti 12, 20133 Milano, Italy

⁹ INAF Osservatorio Astronomico di Trieste, Via G.B. Tiepolo, 11, Trieste 34143, Italy

¹⁰ Scuola Normale Superiore, Piazza dei Cavalieri 7, 56126 Pisa, Italy

¹¹ Dipartimento di Matematica e Fisica, Università Roma Tre, Via della Vasca Navale 84, 00146 Roma, Italy

¹² Dipartimento di Fisica e Astronomia, Università di Bologna, Via Piero Gobetti 93/2, 40129 Bologna, Italy

¹³ INAF-Osservatorio di Astrofisica e Scienza dello Spazio di Bologna, Via Piero Gobetti 93/3, 40129 Bologna, Italy

Received 27 June 2019 / Accepted 15 January 2020

ABSTRACT

Context. In recent years, Ly α nebulae have been routinely detected around high redshift, radio-quiet quasars thanks to the advent of the highly sensitive integral field spectrographs. Constraining the physical properties of the Ly α nebulae is crucial for a full understanding of the circum-galactic medium (CGM). The CGM acts both as a repository for intergalactic and galactic baryons as well as a venue of feeding and feedback processes. The most luminous quasars are privileged test-beds to study these processes, given their large ionising fluxes and dense CGM environments in which they are expected to be embedded.

Aims. We aim to characterise the rest-frame ultraviolet (UV) emission lines in the CGM around a hyper-luminous, broad emission line, radio-quiet quasar at $z \sim 3.6$, which exhibits powerful outflows at both nuclear and host galaxy scales.

Methods. We analyse VLT/MUSE observations of the quasar J1538+08 ($L_{\text{bol}} = 6 \times 10^{47} \text{ erg s}^{-1}$), and we performed a search for extended UV emission lines to characterise its morphology, emissivity, kinematics, and metal content.

Results. We report the discovery of a very luminous ($\sim 2 \times 10^{44} \text{ erg s}^{-1}$), giant Ly α nebula and a likely associated extended (75 kpc) CIV nebula. The Ly α nebula emission exhibits moderate blueshift ($\sim 440 \text{ km s}^{-1}$) compared to the quasar systemic redshift and a large average velocity dispersion ($\sigma_v \sim 700 \text{ km s}^{-1}$) across the nebula, while the CIV nebula shows average velocity dispersion of $\sigma_v \sim 350 \text{ km s}^{-1}$. The Ly α line profile exhibits a significant asymmetry towards negative velocity values at 20–30 kpc south of the quasar and is well parametrised by the following two Gaussian components: a narrow ($\sigma \sim 470 \text{ km s}^{-1}$) systemic one plus a broad ($\sigma \sim 1200 \text{ km s}^{-1}$), blueshifted ($\sim 1500 \text{ km s}^{-1}$) one.

Conclusions. Our analysis of the MUSE observation of J1538+08 reveals metal-enriched CGM around this hyper-luminous quasar. Furthermore, our detection of blueshifted emission in the emission profile of the Ly α nebula suggests that powerful nuclear outflows can propagate through the CGM over tens of kiloparsecs.

Key words. galaxies: active – intergalactic medium – quasars: emission lines – quasars: individual: SDSS 153830.55+085517.0

1. Introduction

In the past few decades, the investigation of extended (tens of kiloparsec-scales) Ly α -emitting nebulae surrounding active galaxies have become more and more intense (see [Cantalupo et al. 2017](#) and references therein). These are a promising

repository for the census of baryonic matter and metals, and they are a privileged environment to study the feeding and feedback processes. The first circum-galactic medium (CGM) emission nebulae detected in Ly α (Ly α -CEN hereafter) were mostly observed around high redshift radio galaxies with sizes exceeding 100 kpc, through narrow-band (NB) imaging and slit spectroscopy (e.g. [Heckman et al. 1991](#); [van Ojik et al. 1997](#); [Villar-Martín et al. 2006, 2007a](#); [Humphrey et al. 2007, 2013](#)). Only a minor fraction ($\sim 10\%$) of them were reported around radio-quiet quasars (RQQs; e.g. [Weidinger et al. 2005](#); [Christensen et al. 2006](#); [Arrigoni Battaia et al. 2016](#)). In rare cases, RQQs have been found lying in overdense active galactic

* The reduced datacube is only available at the CDS via anonymous ftp to [cdsarc.u-strasbg.fr](ftp://cdsarc.u-strasbg.fr) (130.79.128.5) or via <http://cdsarc.u-strasbg.fr/viz-bin/cat/J/A+A/635/A157>

** Based on data obtained with the European Southern Observatory Very Large Telescope, Paranal, Chile, under Programme 099.A-0316(A).

nuclei (AGN) environments and embedded in enormous Ly α nebulae (ELANe) with projected sizes exceeding ~ 200 kpc and surface brightnesses (SB) $> 10^{-17}$ erg s $^{-1}$ cm $^{-2}$ arcsec $^{-2}$ for hundreds of kiloparsecs (Cantalupo et al. 2014; Hennawi et al. 2015; Cai et al. 2017a). Recent sensitive integral field spectrographs, such as VLT/MUSE (Multi Unit Spectroscopic Explorer; Bacon et al. 2010) and Keck/KCWI (Keck Cosmic Web Imager), have recently allowed for the detection of extended Ly α emission around $z = 2-5$ quasars at a depth that has never been explored before and provided a 3D view of Ly α -CEN. Borisova et al. (2016, hereafter B16) and Arrigoni Battaia et al. (2019, hereafter AB19) performed MUSE surveys of optically-bright RQQs at $3 < z < 4$. Also, Cai et al. (2019) used the KCWI to study the CGM surrounding RQQs at $z \approx 2$ and they report detection rates of nearly 100% for Ly α -CEN.

Detailed morphological and kinematic studies of Ly α -CEN reveal that they have large (~ 100 kpc diameter) and mostly symmetrical structures with the bulk of their emission concentrated within tens of kiloparsecs (B16; AB19; Ginolfi et al. 2018; Lusso et al. 2019). Their average SB profiles have been parameterised with exponential (AB19) or power-law (B16) profiles with no clear dependence on radio-loudness (AB19). Although with a few exceptions (e.g. Weidinger et al. 2004, 2005; Cai et al. 2017b; Arrigoni Battaia et al. 2018), Ly α -CEN do not show any clear kinematic pattern (e.g. when ascribed to ordered gas rotation or inflows and outflows) and they exhibit velocity dispersions of $\sigma_v \lesssim 400$ km s $^{-1}$. The latter are consistent with the expected kinematics of their dark matter halo gravitational potential. However, higher σ_v values have been reported for CEN around some RQQs and radio-loud sources (B16; Ginolfi et al. 2018). For the latter, the high σ_v is likely due to the jets mechanical interaction with the Ly α -CEN (van Ojik et al. 1997; Villar-Martín et al. 2006; Silva et al. 2018).

To date, at least three mechanisms have been proposed to explain extended Ly α emission of cold ($T \sim 10^4$ K) gas. The main one is fluorescence, which was predicted for the first time by Hogan & Weymann (1987), whereby the gas emits Ly α photons by recombination when it is photoionised by one or more UV sources (Cantalupo et al. 2005). The second is associated with AGN Ly α photons, which can be resonantly scattered by the neutral hydrogen clouds (Møller & Warren 1998; Cantalupo et al. 2005). Finally, shocks triggered by galactic outflows can power Ly α emission (Taniguchi & Shioya 2000; Arrigoni Battaia et al. 2015a). The contribution of all these mechanisms is expected to be large in the CGM surrounding hyper-luminous ($L_{\text{bol}} \gtrsim 10^{47}$ erg s $^{-1}$) quasars. Indeed, the latter are the most luminous UV emitters (Duras et al. 2017) and sit on large potential wells, which likely suggest the presence of relatively high-density CGM and significant over-density of companions (Bischetti et al. 2018). Furthermore, luminous quasars are also predicted and observed to launch the most powerful winds out to host-galaxy scales (Faucher-Giguère & Quataert 2012; Fiore et al. 2017; Menci et al. 2019). Hence, we can reasonably expect them to affect the kinematics of the CGM and its metal content.

In this paper we report VLT/MUSE observations of SDSS J153830.55+085517.0 (hereafter J1538+08), a hyper-luminous ($L_{\text{bol}} \approx 6 \times 10^{47}$ erg s $^{-1}$) quasar at $z_{\text{QSO}} = 3.567_{-0.002}^{+0.003}$ (based on H β ; Vietri et al. 2018). This source belongs to the WISE/SDSS-selected hyper-luminous quasar (WISSH) sample (Bischetti et al. 2017), that is, the optically and mid-infrared selected most luminous quasars at $z = 2-4$. The WISSH quasars are characterised by pervasive powerful winds from nuclear (Vietri et al. 2018; Bruni et al. 2019) out to kiloparsec scales

(Bischetti et al. 2017) and, hence, they are ideal laboratories for a detailed study of the kinematics and metal content at CGM scales.

The paper is organised as follows: Sects. 2 and 3 describe the reduction of the MUSE data and the methodology for CEN detection, respectively. Section 4 presents the results of our analysis along with the physical properties of the CEN revealed around J1538+08. Section 5 is devoted to the discussion of the Ly α -CEN properties, the presence of metals (i.e. CIV-CEN), and the evidence of an outflow in the CGM traced by the blueshifted Ly α emission. Finally, Sect. 6 reports our conclusions. Throughout the paper we adopt a cosmology with $\Omega_{\Lambda} = 0.68$ and $H_0 = 67.4$ km s $^{-1}$ Mpc $^{-1}$ (Planck Collaboration VI 2018), for which 1 arcsec corresponds to ~ 7.4 kpc at the quasar redshift. All of the errors are quoted at 1σ significance and all flux-weighted quantities were computed for regions with an $S/N \geq 3$, unless stated otherwise.

2. Data reduction

J1538+08 was observed with MUSE on July 26, 2017, as part of the ESO programme ID 099.A-0316(A) (PI F. Fiore). The observation consists of four exposures of 1020 s each, for a total integration time of one hour and eight minutes. Each exposure was rotated by 90° with the addition of a small dithering. The average seeing was ≈ 0.9 arcsec. The data reduction was performed by using the ESO MUSE pipeline (EsoRex v. 3.12.3; Weilbacher et al. 2014) and the code CubExtractor (CubEx v. 1.8; see Cantalupo et al. 2019). We followed a procedure similar to the one reported in B16, which is described in more detail by Cantalupo et al. (2019). We briefly summarise the main steps as follows. For each exposure, we applied bias subtraction and corrected for flat-fielding, twilight, and illumination, using the standard ESO MUSE pipeline. Finally, we applied a wavelength, geometry, and astrometric calibration.

Firstly, we used CubeFix (a tool from the CubExtractor Package) to apply a more accurate flat-fielding correction in each datacube by using the continuum and the emission lines of the sky as calibrators. This procedure consists in deriving the correction factors to be applied to each integral field unit (IFU) and its elements to have coherent values of the sky on the whole field of view (FOV). This allowed us to perform a wavelength and flux dependent correction. The continuum of the sources need to be iteratively masked to minimise the self-calibration errors.

Secondly, we performed a correction of the sky line spread function with the CubeSharp procedure, which adopts a flux-conserving sky-subtraction method (see Cantalupo et al. 2019).

Then, CubEx was used to obtain more refined science datacubes and the associated variances. It is important to note that the standard ESO pipeline can underestimate the propagated variance (Bacon et al. 2017). This variance was therefore propagated during the execution of CubExtractor packages and rescaled by a constant factor to match the empirical spatial variance estimated from the cube at each wavelength layer (see Borisova et al. 2016, for details). The final datacube is a median stack (with 3σ -clipping) of the single datacubes derived from each exposure.

Finally, we notice that during the data reduction with the CubExtractor code, we account for the presence of a saturated bright (Vega magnitude $V \approx 9.7$) star at the edge of the MUSE FOV contaminating large part of the field in each exposure. In the flat-fielding and sky-subtraction, we indeed masked the stellar emission and the bleed trails up to a distance of 16 arcsec

from the quasar where this contribution starts to become negligible for our purposes (see Appendix A for further details).

3. CEN detection methodology

We performed the identification and extraction of the CEN in the final datacube with the `CubeExtractor` package. We first removed the quasar point spread function (PSF) with the `CubePSFSub` task by masking the expected spectral regions that have an extended emission in order to avoid any contamination in the PSF estimation. This recipe estimates the quasar PSF empirically at each wavelength layer from a pseudo-NB image. In our case, each pseudo-NB image was computed with a spectral width of ± 150 pixels, corresponding to ± 188 Å. The estimated PSF was rescaled to its flux in each wavelength layer image and then subtracted. The PSF normalisation was derived by assuming that the central pixels, within a region of $1'' \times 1''$, are quasar dominated. Furthermore, we removed the continuum emission of any source within the MUSE FOV by means of a fast median-filtering approach using the `CubeBKGSub` task (see [Cantalupo et al. 2019](#) for further details).

We searched for diffuse emission in the PSF- and continuum-subtracted datacube with the `CubeEx` recipe. The latter allowed us to detect and extract extended sources by applying a connected labelling component algorithm. The key input parameters of this algorithm are N_{\min}^{vox} and S/N_{th} , which define the minimum number of connected voxels and the signal-to-noise ratio (S/N) threshold of the extended emission that is to be searched for, respectively. `CubeEx` returns astrometric, photometric, and spectroscopic information on the extended nebular emissions and generates both a three-dimensional mask (3D-mask), which defines the datacube elements (i.e. voxels) belonging to the detected nebula, and a 3D S/N cube. Once the CEN was detected and extracted, the `Cube2Im` task allowed us to create, for the detected CEN, the following three data products by using the voxels of the PSF- and continuum-subtracted datacube defined in the 3D-mask: (i) the SB map, that is, an “optimally extracted image” derived by applying the 3D-mask to the datacube and by collapsing, at each spaxel, the contribution of the nebula voxels above the chosen S/N_{th} ; (ii) a map of the velocity distribution obtained as the first moment of the flux distribution; and (iii) a map of σ_v , which was derived as the second moment of the flux distribution. All these data products were smoothed with a Gaussian-kernel of $\sigma = 2$ pixels (0.4 arcsec). We computed the S/N map from the pseudo-NB image obtained by collapsing the wavelength range (i.e. the layers) in which the extended emission was detected to have an estimation of the variance distribution of the SB map. Then we associated an S/N value to each pixel, where the noise is the average of the standard deviations derived in several background regions with a size of $1'' \times 1''$. The S/N map was finally smoothed with a Gaussian-kernel of $\sigma = 2$ pixels, in order to be consistent with the smoothing of the maps produced by `Cube2Im`.

4. Results

We searched for CEN around J1538+08 traced by typical CGM UV transitions, such as $\text{Ly}\alpha$ $\lambda 1215$ Å, $\text{NV}\lambda 1240$ Å, $\text{SiIV}\lambda 1397$ Å, $\text{CIV}\lambda 1549$ Å, $\text{HeII}\lambda 1641$ Å, and $\text{CIII]}\lambda 1909$ Å. We detected significant nebular emission in $\text{Ly}\alpha$ and CIV. The properties of the detected CEN are described in the following sections.

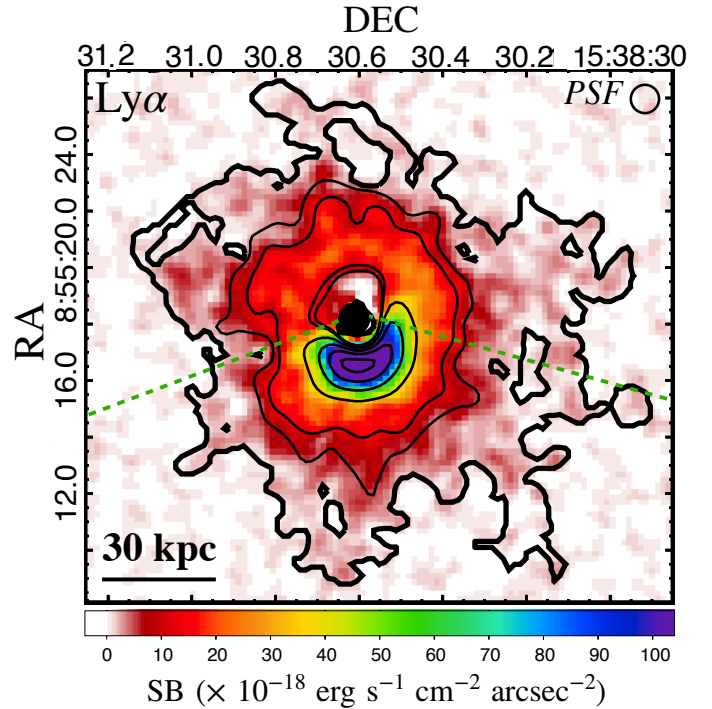


Fig. 1. Optimally extracted SB map of the $\text{Ly}\alpha$ -CEN. The quasar position is marked by a black dot. The thick black contour corresponds to the two-dimensional projection of the boundary of the CEN from the 3D-mask. It indicates an SB level of about $10^{-18} \text{ erg s}^{-1} \text{ cm}^{-2} \text{ arcsec}^{-2}$. The thin black contours indicate the S/N levels 3, 5, 15, 25, 35, and 45 extracted from the S/N map. The wavelength layer at the $\text{Ly}\alpha$ profile peak is used to report the background fluctuations in the image. On the top-right corner, the circle indicates the size of the FWHM of the instrument PSF. The green dashed lines delimit two regions of the $\text{Ly}\alpha$ -CEN (i.e. north and south from the quasar position) used for the extraction of the radial profile (see Fig. 3). The low-S/N region close to the quasar with SB values around zero could be the result of either random fluctuations or real features of the distribution of the CGM gas emission.

4.1. $\text{Ly}\alpha$ nebula

We found a $\text{Ly}\alpha$ -CEN consisting of $\sim 55\,000$ connected voxels by using $S/N_{\text{th}} = 2.5$ and $N_{\min}^{\text{vox}} = 10\,000$ pixels. This CEN exhibits a maximum angular extension of ~ 20 arcsec (~ 150 kpc). The line emission integrated over the entire CEN spans a maximum wavelength range of ~ 95 Å ($\sim 5000 \text{ km s}^{-1}$) and shows a peak measured through a Gaussian fit at $\lambda_{\text{Ly}\alpha}^{\text{CEN}} = (5543.8 \pm 1.8) \text{ Å}$. This corresponds to a redshift of $z_{\text{CEN}}^{\text{Ly}\alpha} = 3.560 \pm 0.002$.

Figure 1 shows the SB map of the $\text{Ly}\alpha$ -CEN. The nebular emission is the region enclosed in the black thick contour, that is, the projected boundary derived from the 3D-mask, which encloses the detected CEN with $S/N > 2.5$. The thin contours indicate the S/N levels derived from the S/N map. This $\text{Ly}\alpha$ -CEN exhibits a roughly symmetric shape on large scales suggesting a circular, or mildly elliptical, morphology with marked deviations at small radii. In order to obtain a more quantitative description of its morphology, we computed the flux weighted centroid shift ($d_{\text{CEN}}^{\text{cen}}$), the peak displacement ($d_{\text{CEN}}^{\text{peak}}$), the asymmetry (α), and the position angle east of north (ϕ) of the CEN. The first two quantities were measured with respect to the quasar position, while the remaining ones were estimated from the Stokes parameters as in AB19 (see Table 1). We find general

Table 1. Physical properties of the detected CEN.

	Ly α	CIV
$\lambda_{\text{CEN}} [\text{\AA}]$ ^(a)	5543.8 ± 1.8	7064.7 ± 1.8
z_{CEN} ^(b)	3.560 ± 0.002	3.559 ± 0.001
Size [kpc] ^(c)	150	75
Spectral width [\AA] ^(d)	95	42
$d_{\text{CEN}}^{\text{peak}}$ [kpc] ^(e)	10.4 ± 3.7 (*)	15.1 ± 3.7 (*)
$d_{\text{CEN}}^{\text{cen}}$ [kpc] ^(f)	5.7 ± 3.7 (*)	13.7 ± 3.7 (*)
α ^(g)	0.72	0.62
ϕ [degree] ^(h)	62	11
Flux [$\times 10^{-16}$ erg s $^{-1}$ cm $^{-2}$] ⁽ⁱ⁾	17.8 ± 0.1	0.77 ± 0.03
Luminosity [$\times 10^{43}$ erg s $^{-1}$] ^(j)	20.55 ± 0.16	1.00 ± 0.03
$\bar{\sigma}_v$ [km s $^{-1}$] ^(k)	770 ± 2	352 ± 7
$\bar{\sigma}_g$ [km s $^{-1}$] ^(l)	560 ± 15	455 ± 55

Notes. ^(a)Line peak wavelength from the Gaussian modelling of Ly α - and CIV-CEN spectrum. ^(b)Redshift of the CEN corresponding to λ_{CEN} . We used as Ly α and CIV λ rest-frame 1215.67 \AA and 1549.48 \AA , respectively. ^(c)Maximum projected physical size derived from the 3D-mask. ^(d)Spectral width within which the CEN was detected (from 3D-mask). ^(e)Distance from the quasar position to the SB peak of the CEN. ^(f)Distance from the quasar position to the flux weighted centroid of the CEN. ^(g)Asymmetry parameter, i.e. the ratio between the semi-minor and semi-major axis of the SB map. ^(h)Position angle east of north of the major axis of the SB map. ⁽ⁱ⁾Total flux derived from the SB maps (Figs. 1 and 4). ^(j)Total CEN luminosity. ^(k)Averaged velocity dispersion measured from the $S/N \geq 3$ velocity dispersion maps (see Sect. 4.3) of the Ly α and CIV. ^(l)Velocity dispersions derived from the Gaussian fit of the total Ly α - and CIV-CEN spectrum. (*)Errors according to the spatial resolution of MUSE data.

consistency with morphological properties reported by AB19 in the QSO MUSEUM sample. Indeed, both the flux-weighted centroid shift and the asymmetry measured for the Ly α -CEN around J1538+08 are close to the median values reported in AB19, that is, 8.3 kpc and 0.71, respectively. The Ly α -CEN exhibits a maximum SB value of $\sim 10^{-16}$ erg s $^{-1}$ cm $^{-2}$ arcsec $^{-2}$ and a total luminosity of $L_{\text{Ly}\alpha} = (2.06 \pm 0.02) \times 10^{44}$ erg s $^{-1}$.

The comparison between the Ly α spectra of the quasar and the CEN normalised to their peak emission is shown in Fig. 2. The quasar spectrum was extracted from an aperture with a radius of 3 arcsec, while the CEN spectrum was obtained from the PSF, and continuum, subtracted datacube by summing the spectral contribution of all the spaxels belonging to the CEN (i.e. from the 3D-mask). The x -axis reports the velocity relative to z_{QSO} . The white area in the plot corresponds to the spectral width where the CEN was detected (i.e. the maximum spectral extent of the 3D mask; see also Table 1). The red area marks the peak of the Ly α profile of the CEN and includes the errors. The measure of the peak has been obtained through a Gaussian modelling plus a constant continuum term, performed within a range ± 500 \AA (or $\pm 27\,000$ km s $^{-1}$) from the Ly α wavelength at z_{QSO} . This peak appears to be reasonably (i.e. at $\sim 1\sigma$) consistent with the z_{QSO} and its 1σ uncertainty (yellow area in Fig. 2).

Figure 3 reports the circularly averaged radial SB profile of the Ly α -CEN in J1538+08 (black points), which was corrected for minimal residual background emission¹. The profile

¹ Similar to B16, the SB is estimated at scales much larger than the CEN and the profile is corrected for possible residual background due to unresolved and faint background or foreground (see Appendix A) emission that was not removed during the continuum subtraction. This

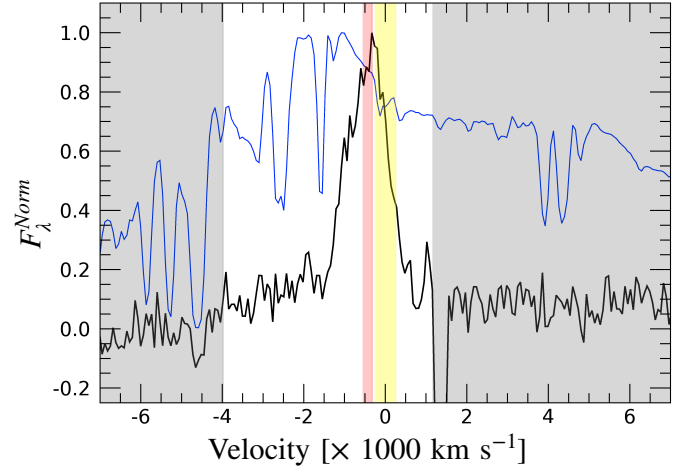


Fig. 2. Black and blue represents the Ly α emission lines in the CEN and quasar spectrum, respectively. These Ly α line spectra are reported in velocity space relative to the z_{QSO} and they both are normalised to their peak. The white region reports the spectral range of the 3D-mask. The red area marks the peak wavelength of the Ly α line derived through Gaussian modelling including the errors. The yellow area indicates the 1σ uncertainty of the systemic redshift of the quasar (Vietri et al. 2018). The absorption line at ~ 1500 km s $^{-1}$ is a sky feature, which could not be appropriately removed by the algorithm CubePSFSub.

was extracted from concentric annular regions centred on the quasar position in the image obtained by collapsing the spectral region in the CEN 3D-mask. The grey area indicates the 2σ Poisson noise². The radial profile was compared to the average radial profiles reported by B16 and AB19. All of the SB radial profiles in Fig. 3 were corrected for the cosmological $(1+z)^4$ SB dimming factor and re-scaled at $z=3$ for comparison purposes.

We also report the rescaled profile of the CEN around the quasar J0124+00 (also belonging to the WISSH quasar sample, e.g. Duras et al. 2017), which was identified by B16 as the brightest and most peculiar one in their sample in terms of sharp-peaked morphology, large velocity dispersion, and SB radial profile. Both the Ly α -CEN around these WISSH quasars exhibit a central (i.e. <40 – 50 kpc) SB excess relative to the B16 and AB19 average profiles.

We further investigated the origin of this SB excess in J1538+08 by comparing the radial profiles extracted for two regions, that is, south and north of the quasar, which are delimited by the green dashed lines in Fig. 1. Accordingly, the southern region includes the SB peak of the Ly α -CEN and the CIV-CEN (see Fig. 4). The SB excess is clearly due to the contribution from the southern region (blue triangles in Fig. 3) at ≤ 20 kpc, while both regions equally contribute to the SB excess at larger radii.

4.2. CIV nebula

We scanned the datacube searching for diffuse emission in additional ionic transitions that typically probe the CGM. The only

subtraction, which was performed for both the Ly α and the CIV profiles (see Sect. 4.2), was measured to be negligible accounting for 5–15% of the flux of the most external annuli (used for the SB profile) placed at the boundary of each CEN.

² The Poisson noise was estimated as the average value of the standard deviations within background regions $1'' \times 1''$ of the pseudo-NB divided by the square root of each annulus area.

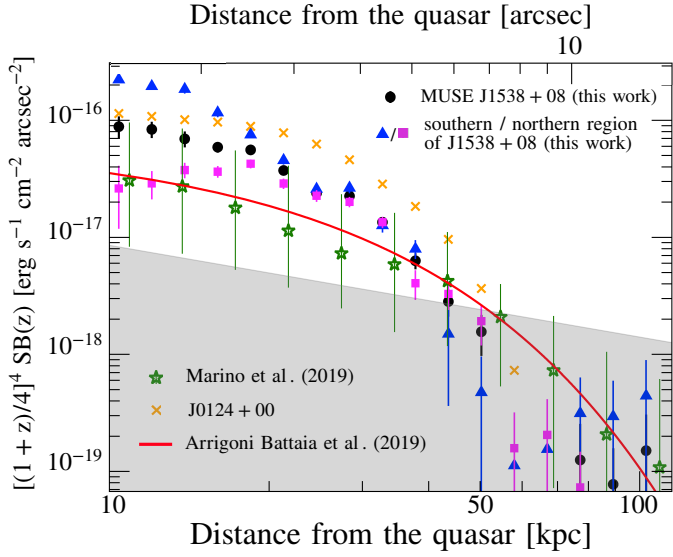


Fig. 3. $\text{Ly}\alpha$ SB radial profile (black circles) of the pseudo-NB image. The points represent bins of SB measured in concentric annuli centred on the quasar position and their errors indicate the 16th and 84th percentile, which corresponds to $\sim 68\%$ of the SB distribution centred on the median value (i.e. $\pm 1\sigma$ for a Gaussian distribution). The bin width is chosen to be uniformly spaced in a logarithmic scale. The blue triangles and magenta squares show the radial profiles measured in the southern and northern region of the CEN, respectively (see Fig. 1). The red curve is the modelled average radial profile of the AB19 quasar sample. We also include the average radial profile of the $\text{Ly}\alpha$ -CEN of the sample of B16, which was recalculated by Marino et al. (2019) (the error bars represent the 25th and 75th percentiles). The orange crosses represent the radial profile of the $\text{Ly}\alpha$ -CEN around the WISSH quasar J0124+00 in the B16 sample. All the SB profiles were corrected for the cosmological dimming effect and re-scaled at $z = 3$ (i.e. $[(1+z)/4]^4 \times \text{SB}(z)$). The grey shaded area indicates the 2σ Poisson noise relative to the rescaled profiles of the $\text{Ly}\alpha$ -CEN around J1538+08 (see Sect. 4.1 for details). We verified that the decline of the SB radial profile from the northern region (magenta squares) at short radius towards the centre is not due to the white region immediately north of the quasar (see Fig. 1).

extended emission detected at a good significance level is traced by the CIV line. Given its typically lower emissivity compared to the $\text{Ly}\alpha$, we started our search by setting $S/N_{\text{th}} = 2.5$ and $N_{\text{th}}^{\text{vox}} = 10\,000$ and then progressively lowered $N_{\text{th}}^{\text{vox}}$ by steps of 1000 voxels until the extended emission was detected. We found that the $N_{\text{th}}^{\text{vox}} = 4000$ was required to detect this CEN, which indeed consists of 4726 voxels.

The SB map of the CIV-CEN is shown in Fig. 4. The CIV-CEN is much smaller than the $\text{Ly}\alpha$ -CEN, with a maximum angular extension of ~ 10 arcsec, which corresponds to a projected physical size of ~ 75 kpc. It is almost completely contained in the southern region and exhibits an asymmetric morphology with $\alpha = 0.62$. The peak of the SB_{CIV} is located roughly at the same position of the $\text{SB}_{\text{Ly}\alpha}$ peak at a distance of $\sim 11.0 \pm 3.5$ kpc from the quasar position. The value of the SB peak ($\sim 10^{-17}$ erg s $^{-1}$ cm $^{-2}$ arcsec $^{-2}$) and the luminosity of the CIV-CEN ($L_{\text{CIV}} = (9.33 \pm 0.33) \times 10^{42}$ erg s $^{-1}$) are one order of magnitude lower than those measured for the $\text{Ly}\alpha$ -CEN.

Figure 5 shows the comparison between the CIV emission line in the CEN and the quasar spectrum. The CIV-CEN was detected in a relatively narrow spectral range (~ 2000 km s $^{-1}$) compared to the spectral region of the $\text{Ly}\alpha$ -CEN (~ 5000 km s $^{-1}$). Through Gaussian modelling of the line (similar to the one performed for the $\text{Ly}\alpha$), we found that the CIV line peaks at

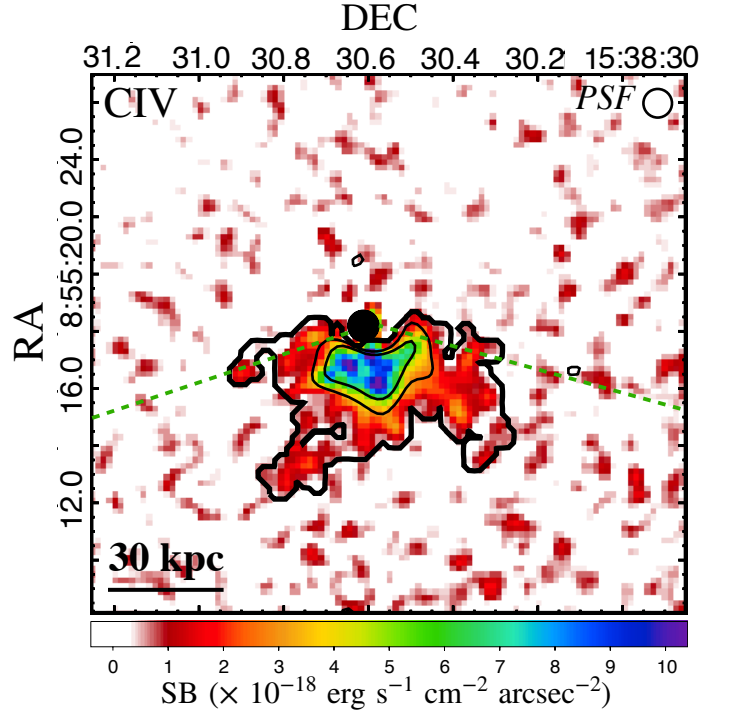


Fig. 4. Optimally extracted SB map of the CIV-CEN. The black dot, the contours, and the dashed green lines have the same meaning as in Fig. 1. Thin contours report levels of $S/N = 3$ and 5.

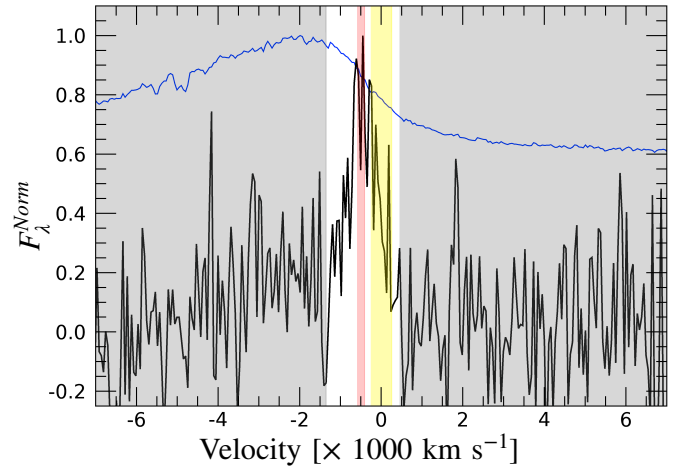


Fig. 5. Spectrum of the CIV emission as a function of the velocity with respect to the quasar redshift of the CIV-CEN (black) and quasar (blue) normalised to their peak emission. Labelling and symbols are the same as in Fig. 2.

$\lambda_{\text{CIV}}^{\text{CEN}} = 7064.7 \pm 1.8 \text{ \AA}$. This corresponds to a redshift of $z_{\text{CIV}}^{\text{CEN}} = 3.559 \pm 0.001$, which is in good agreement with the $\text{Ly}\alpha$ -CEN one. We computed the SB radial profile of the CIV emission (Fig. 6) in the southern region. The emission of the CEN is clearly above the Poisson noise up to ~ 20 kpc from the quasar position.

4.3. Kinematic properties of the CEN

Figures 7 and 8 show the flux-weighted velocity maps in regions with $S/N \geq 3$ for the $\text{Ly}\alpha$ - and CIV-CEN, respectively. Each panel reports the velocities relative to the CEN (z_{CEN} ; left panel) and z_{QSO} (right panel) rest-frame, respectively. There is

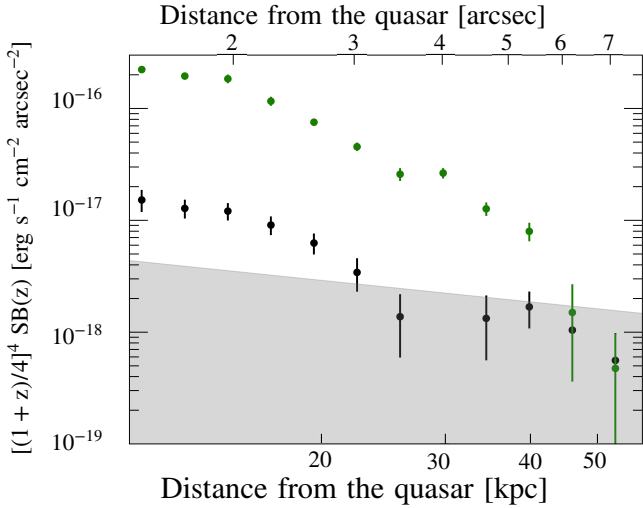


Fig. 6. SB radial profile of the CIV-CEN (black) extracted in the southern region (see Fig. 4). The SB profile for the Ly α -CEN, extracted in the same region, is also reported in green. These profiles are re-scaled at $z = 3$ and corrected for the cosmological dimming effect. For other details refer to the caption of Fig. 3.

no significant structure indicative of bulk motion or clear separation between red and blueshifted gas components. Interestingly, almost the entire Ly α -CEN exhibits velocities spanning $\sim 1000 \text{ km s}^{-1}$.

We also investigated the radial velocity profile of the Ly α -CEN to assess a possible trend with the distance from the quasar. Specifically, we extracted spectra from the PSF- and continuum-subtracted datacube in each annular region used for the SB radial profiles (see Fig. 3). For each spectrum, we modelled the Ly α emission line with a Gaussian profile. Figure 9 shows the radial distribution of the best-fit velocities relative to the z_{CEN} (blue points). The velocity profile exhibits a constant value around $\sim 100\text{--}200 \text{ km s}^{-1}$ up to $15\text{--}20 \text{ kpc}$. There is an apparent decline of the velocity down to $\sim 200 \text{ km s}^{-1}$ at larger radii ($20\text{--}30 \text{ kpc}$).

The flux-weighted velocity dispersion maps for Ly α - (left panel) and CIV-CEN (right panel) are shown in Fig. 10. For the Ly α -CEN, we do not notice any specific gradient as the map shows a nearly constant σ_v in the range of $600\text{--}900 \text{ km s}^{-1}$ with few regions reaching values larger than 1000 km s^{-1} . In case of the CIV-CEN, the map shows a factor of 2 lower velocity dispersions than the Ly α -CEN. Table 1 lists the average velocity dispersions ($\bar{\sigma}_v$) obtained from these maps. The dispersion estimated through Gaussian model fitting ($\bar{\sigma}_g$) of the total spectrum of the Ly α - and CIV-CEN is also reported.

In order to better explore the possible presence of a radial gradient of the Ly α emission velocity dispersion, we computed the radial dispersion profile by using the same methodology adopted for the velocity profile (see red points in Fig. 9). The profile exhibits $\sigma_v \sim 500 \text{ km s}^{-1}$ up to $\sim 15\text{--}20 \text{ kpc}$ and an increase of up to $\sigma_v \sim 900 \text{ km s}^{-1}$ at $\sim 25 \text{ kpc}$ from the quasar. The profiles could only be accurately computed up to 40 kpc since the line profile modelling at larger distances is completely unconstrained.

4.4. CIV/Ly α and HeII/Ly α line ratios

We derived a CIV/Ly α line flux ratio of 0.06 ± 0.01 , which is in agreement with the approximate values previously estimated for some tentative ($\sim 2.2\sigma\text{--}2.8\sigma$) detections of CIV-CEN in B16.

Similar to our result, the B16 values were obtained by estimating the total flux of the voxels associated with the Ly α 3D-Mask shifted at the wavelength of the CIV corresponding to z_{CEN} , which was divided by the total flux of the Ly α -CEN (reported in Table 1). This procedure avoids the bias due to aperture effects (i.e. different extensions for different line emissions), and it provides a conservative estimate if the Ly α -CEN is the brightest and more extended one, which is to be expected.

The CIV/Ly α ratio map reported in Fig. 11 is the ratio between the CIV and Ly α SB maps over the $S/N \geq 3$ regions. The spatial distribution of the ratios suggests that the metal distribution is not completely homogeneous. The median value of the CIV/Ly α ratio directly measured from the CIV/Ly α map is $0.08^{+0.11}_{-0.04}$, where the uncertainties are derived by the 16th and 84th percentiles (corresponding to $\pm 1\sigma$ for a Gaussian distribution). A consistent value was obtained by computing the S/N-weighted average of the map values of both Ly α - and CIV-CEN.

No HeII emission line is visible in the quasar spectrum and no HeII-CEN is detected around J1538+08 at z_{CEN} . This is not surprising: While extended HeII emission is commonly observed around high-redshift radio galaxies (e.g. Wilman et al. 2000; Villar-Martín et al. 2007a), it is only found in 6% of the RQQs in the B16 sample. We inferred a 2σ upper limit to the HeII/Ly α ratio of <0.02 by applying the same Ly α 3D-mask shift procedure used to obtain the total CIV/Ly α flux ratio.

4.5. Asymmetry in Ly α line profile

The integrated profile of the Ly α emission line extracted from the entire CEN and reported in Fig. 2 exhibits a blue tail, which can be modelled by an additional component with negative velocity. With the aim of exploring the spatial distribution of this blue tail component, we mapped the asymmetry of the Ly α emission line profile by using the skewness estimator (sk). As for the velocity and dispersion maps, we derived the skewness map as the third moment of the flux distribution according to the following formula:

$$\text{skewness} = \frac{\sum_{i,j,k}^{\text{3D-Mask}} \text{Residuals}_{i,j,k}^3 \times F_{i,j,k}}{M_2^{3/2} \times \sum_{i,j,k}^{\text{3D-Mask}} F_{i,j,k}} \quad (1)$$

where $\sum_{i,j,k}^{\text{3D-Mask}}$ is the sum on each voxel defined in the 3D-Mask, $F_{i,j,k}$ is the PSF and continuum-subtracted flux from the datacube, and M_2 is the second moment of the flux distribution, defined as:

$$M_2 = \frac{\sum_{i,j,k}^{\text{3D-Mask}} \text{Residuals}_{i,j,k}^2 \times F_{i,j,k}}{[\sum_{i,j,k}^{\text{3D-Mask}} F_{i,j,k}]^2 - [\sum_{i,j,k}^{\text{3D-Mask}} F_{i,j,k}^2]} \quad (2)$$

We find that the southern part of the CEN, which has skewness values of $sk < -0.5$ (blue regions in Fig. 12), overlaps with the region of high SB. We verified that other regions do not exhibit skewness at significant levels (i.e. mostly symmetric and low S/N line profiles). The Ly α spectrum extracted from spaxels with $sk < -0.5$ and $S/N \geq 3$ resulted to be clearly asymmetric (Fig. 13). We fitted it with two Gaussian components and an additional constant term to account for residual background. The two Gaussian components exhibit significantly different width, with the broad ($\sigma_v \approx 1170 \pm 260 \text{ km s}^{-1}$) component blueshifted by $v_{\text{shift}} = 1520 \pm 360 \text{ km s}^{-1}$ and the narrow one ($\sigma_v \approx 470 \pm 70 \text{ km s}^{-1}$, see Table 2) tracing the systemic z_{QSO} . The velocity dispersion found for the narrow component is comparable to the ones reported in Ly α -CEN around high- z RQQs